



Near-field radiative heat transfer in scanning thermal microscopy computed with the boundary element method



K.L. Nguyen*, O. Merchiers, P.-O. Chapuis

Univ Lyon, CNRS, INSA-Lyon, Université Claude Bernard Lyon 1, CETHIL UMR5008, F-69621, Villeurbanne, France

ARTICLE INFO

Article history:

Received 14 February 2017

Revised 29 May 2017

Accepted 20 July 2017

Available online 21 July 2017

Keywords:

Near-field radiative heat transfer

Scanning thermal microscopy

Boundary element method

ABSTRACT

We compute the near-field radiative heat transfer between a hot AFM tip and a cold substrate. This contribution to the tip-sample heat transfer in Scanning Thermal Microscopy is often overlooked, despite its leading role when the tip is out of contact. For dielectrics, we provide power levels exchanged as a function of the tip-sample distance in vacuum and spatial maps of the heat flux deposited into the sample which indicate the near-contact spatial resolution. The results are compared to analytical expressions of the Proximity Flux Approximation. The numerical results are obtained by means of the Boundary Element Method (BEM) implemented in the SCUFF-EM software, and require first a thorough convergence analysis of the progressive implementation of this method to the thermal emission by a sphere, the radiative transfer between two spheres, and the radiative exchange between a sphere and a finite substrate.

© 2017 Elsevier Ltd. All rights reserved.

1. Introduction

Radiative heat transfer in the far field [1], *i.e.* for inter-object distances larger than Wien's wavelength ($\sim 10\ \mu\text{m}$ at room temperature), is well established. In contrast, near-field radiative heat transfer (NFRHT), when the gap size between objects is smaller than Wien's wavelength, is a relatively new field. It was realized few decades ago that near-field radiative effects can have an impact on the local temperature or on the heat flux transfer in scanning probe microscopy (SPM) techniques [2]. It is especially important for scanning thermal microscopy (SThM), a technique which aims at measuring local temperature or thermal properties. To understand these local measurements, a precise knowledge of all the heat transfer mechanisms between the SThM tip and the sample under study is required [3]. The contribution of near-field thermal radiation has been so far the hardest to estimate accurately due to a lack of reliable theoretical methods able to deal with complex geometries. Nevertheless, this contribution is critical when the tip is not in contact, in particular when the SThM is operated in vacuum. Tip-sample near-field heat transfer has received increasing attention during the last decade thanks to technical advances allowing experiments with improved thermal sensitivity down to the sub-nW.K⁻¹ regime [4–8]. Recently, such experiments have been carried out to measure radiative heat transfer in the last few nanometers before contact [7–9]. Other SPM techniques, such as Thermal

Radiation Scanning Tunneling Microscopy (TR-STM) [10,11], where the near field is scattered and detected in the far field, therefore providing sub-wavelength information on the sample [10], are also impacted by heat transfer between the probe and the sample. Obviously, various SPM techniques could also benefit from improved theoretical methods to predict NFRHT between complex objects.

NFRHT was quantified by analytical and numerical methods in various configurations. Since the seminal case of two half-spaces [12], analytical methods were developed to quantify the heat transfer between academic configurations involving planar media and dipoles, spheres, cylinders (see *e.g.* respectively [4,13–15]). These approaches are, however, limited to simple geometries. Numerical methods used in NFRHT are based on those for electromagnetic wave scattering and propagation. The Finite Difference Time Domain (FDTD) method [16] was used for computing the heat exchanged between arbitrary geometries in a statistical manner. It consists in applying the fluctuation-dissipation theorem to the Poynting vector averaged over many simulations by considering the random values of surface currents. The drawbacks of this method are the long computational time and the accuracy of the numerical results due to various numerical errors such as discretization of objects and numerical dispersion intrinsic to the space-time scheme. The radiative heat transfer can be also computed by implementing the Thermal Discrete Dipole Approximation (T-DDA) and the Bulk Field Formulation of Electromagnetism (BUFF-EM) methods. The T-DDA method was proposed initially for modelling radiative heat transfer between three-dimensional arbitrary compact objects [17] and then extended to finite-size object close to an infinite surface [18]. This method consists in discretizing

* Corresponding author.

E-mail address: khac-long.nguyen@insa-lyon.fr (K.L. Nguyen).

the objects in sub-volumes, each considered as a thermally oscillating dipole. The BUFF-EM is a free, open-source software implementation of the frequency-domain volume-integral-equation (VIE) method of classical electromagnetic scattering [19,20]. It consists in modelling the bodies by volume (tetrahedral) meshes. The last approach we will discuss is based on the surface-integral-equation (SIE) formulation of classical electromagnetism that allows direct application of the boundary element method (BEM) [21]. It attracted a lot of attention because it offers considerable flexibility to handle arbitrary shapes. Contrary to the T-DDA and BUFF-EM methods, it requires to discretize the surface and not the volume, so that less mesh elements could be required. In this work, we use the implementation of this approach provided in the open-source SCUFF-EM software package developed at MIT [22]. It was already used in [7,8] for the analysis of the tip-sample radiative heat transfer, but not in a comprehensive way.

The paper is organized in two main parts devoted (i) to the SCUFF-EM computations (Sections 2 and 3) and (ii) to the AFM tip-sample radiative heat transfer (Section 4). We first perform calculations of thermal radiative emission and radiative transfer involving homogeneous spheres in Section 2 to validate the SCUFF-EM code against asymptotic formulae. Section 3 deals with thermal transfer between a sphere and a planar substrate. This configuration is of interest in scanning thermal microscopy where the probe tip can sometimes be approximated by a sphere [7,11,23]. Furthermore, spheres attached to tips have been used for experimental investigations of near-field thermal radiation [4,5]. This section explains which requirements are needed to simulate a planar surface. Sections 2 and 3 analyse numerical convergence and could be used as a guide for future computations with SCUFF-EM for other geometries. The final section introduces the numerical modelling of heat transfer between a conical probe tip and a planar substrate. The dependence of heat transfer on the gap size between a compact object (sphere or tip) and a substrate is studied in Sections 3 and 4 for highlighting the near-field characteristics. Finally we compare the flux levels computed with recent experiments and investigate the shape of the heat flux distribution on top of the sample in order to determine the spatial resolution of radiative heat transfer. This is done for two typical radii of curvature. The numerical results are compared to predictions of the Proximity Flux Approximation [24] (also called the Derjaguin approximation).

2. Validation of SCUFF-EM

In this section, the accuracy of the SCUFF-EM code as a function of object and mesh size will be compared with known analytical results. SCUFF-EM is a free, open-source software implementation of the boundary-element method (BEM) for electromagnetic scattering. SCUFF-NEQ is an application code in the SCUFF-EM suite for studying non-equilibrium (NEQ) electromagnetic-fluctuation-induced phenomena. It gives the radiative heat transfer or emission rates for bodies of arbitrary shapes (spheres, cylinders, interlocked rings, conical shapes [7,21,25], etc.) and arbitrary (linear, isotropic, piecewise homogeneous) frequency-dependent permittivity and permeability. The numerical calculations were performed on the P2CHPD cluster (high-performance computing facility at Université Claude-Bernard Lyon 1). Many nodes may be used for parallel or sequential computing. Each node has 64 GB RAM and two processors with 16 cores Intel(R) Xeon(R) CPU E5-2670@2.6 GHz.

We first consider thermal radiative emission and radiative transfer involving homogeneous spheres, the simplest compact objects. Thermal emission by a homogeneous sphere is known analytically, in a framework related to Mie theory [26,27].

2.1. Thermal emission of a sphere

The thermal radiation power emitted by a sphere is given by

$$Q_{\text{rad}}(T) = \int_0^\infty \Theta(\omega, T) \tau_{\text{rad}}(\omega, R) d\omega \quad (1)$$

where R is the sphere radius, $\Theta(\omega, T) = \frac{\hbar\omega}{e^{\frac{\hbar\omega}{k_B T}} - 1}$ is the mean energy of the Planck oscillator at temperature T and τ_{rad} denotes a temperature-independent dimensionless transmittivity that can be computed using the Mie coefficients [26,27].

In this work, only isothermal objects are studied. Two materials are considered: SiO₂ and SiC. The optical properties of SiO₂ are taken from Ref. [28]. The dielectric function of SiC is given by

$$\varepsilon(\omega) = \varepsilon_\infty \left(1 + \frac{\omega_L^2 - \omega_T^2}{\omega_T^2 - \omega^2 - i\Gamma\omega} \right)$$

where $\varepsilon_\infty = 6.7$, $\omega_L = 1.825 \times 10^{14}$ rad.s⁻¹, $\omega_T = 1.494 \times 10^{14}$ rad.s⁻¹ et $\Gamma = 8.966 \times 10^{11}$ rad.s⁻¹.

We first consider a single SiC sphere. Fig. 1a compares the spectrum of τ_{rad} of the SiC sphere of radius 0.1 μm, computed for two different meshes, and the results obtained by the analytical model (black curve). Blue crosses correspond to the numerical results obtained for a coarse mesh which consists of 172 nodes and 507 edges with a mesh element size of 0.035 μm. Red circles are the numerical results for the finer mesh with 494 nodes and 1473 edges with a mesh element size of 0.017 μm. We note that τ_{rad} shows two maxima close the SiC resonance ($\varepsilon(\omega) = -2$ for $\omega \simeq 1.5 \times 10^{14}$ rad.s⁻¹ and $\omega \simeq 1.75 \times 10^{14}$ rad.s⁻¹). For each frequency, the computation takes 12 s for the coarse mesh and 25 min for the fine mesh. From Fig. 1a, the numerical results are in good agreement with analytical results. As expected, Fig. 1b represents the relative error of numerical results compared to analytical ones. The numerical results converge as the mesh gets finer. However, the relative error stays around 20% close to the resonance and does not decrease when the mesh size is decreased.

Fig. 2a represents τ_{rad} of a smaller SiC sphere of radius 0.0125 μm. Similarly to the previous test case, two meshes are considered: one containing 172 nodes and 507 edges with a mesh element size of 0.004 μm, and another one consisting of 492 nodes and 1467 edges with a mesh element size of 0.002 μm. The relative error is shown in Fig. 2b. Numerical results for the coarse mesh (blue crosses) are consistent with analytical results except in the low-frequency range. These results become worse for the fine mesh because there is an inherent numerical difficulty for the computation at low frequencies or for very small objects, typically for the case where the ratio between the element size and the wavelength is lower than 2×10^{-4} . We will therefore need to pay attention to this point in what follows.

The refractive index $n = \text{Re}(n) + i\text{Im}(n)$ sets two characteristic lengths $\lambda/\text{Re}(n)$ and $\lambda/\text{Im}(n)$ to which the mesh size should be compared. As a result, we now study the effect of the refractive index n on the convergence by analyzing the variation of τ_{rad} of a sphere of 10 μm radius for different meshes at a given frequency 1.88×10^{14} rad.s⁻¹ (the wavelength in vacuum is 10 μm). Two meshes are considered, with mesh element sizes $\Delta x = 1$ μm and $\Delta x = 2$ μm. Fig. 3a represents the relative error as a function of the ratio between Δx and the wavelength in the sphere $\lambda/\text{Re}(n)$, for $\text{Im}(n) = 0.01$ with $\text{Re}(n)$ varying from 10^{-3} to 10^3 . Fig. 3b shows the relative error as a function of the ratio between Δx and the penetration depth $\lambda/(2\pi\text{Im}(n))$, for $\text{Re}(n) = 1$ with $\text{Im}(n)$ varying from 10^{-2} to 10^4 . Red curves correspond to the results for the coarse mesh and blue curves are results obtained for the fine mesh. We observe that when the mesh size is reduced twice, relative errors decrease three times while the computational

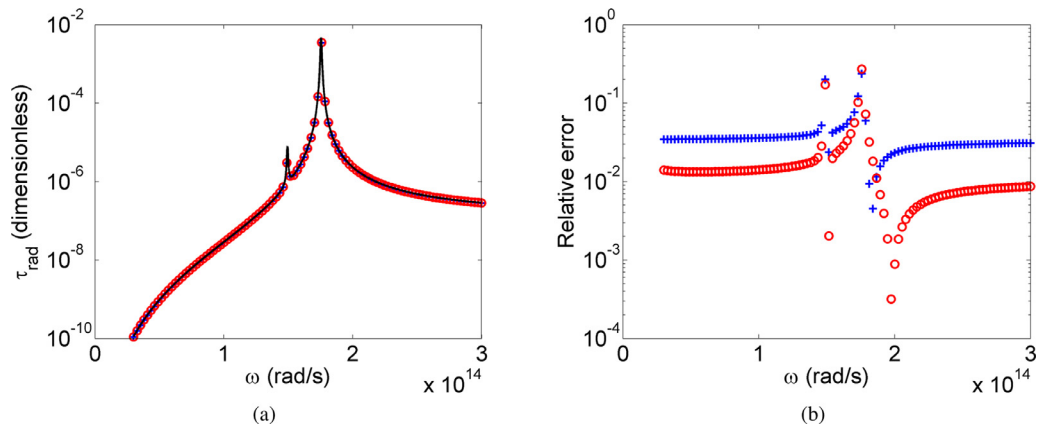


Fig. 1. (a) τ_{rad} of a SiC sphere of radius $0.1 \mu\text{m}$, (b) relative errors. Blue crosses: numerical results for a coarse mesh, red circles: numerical results for a fine mesh, black curve: analytical results. (For interpretation of the references to color in this figure legend, the reader is referred to the web version of this article.)

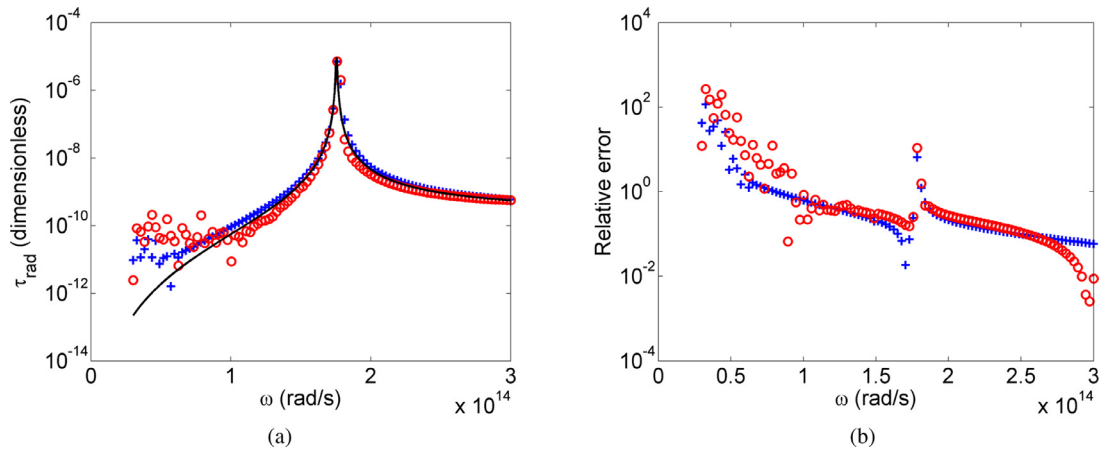


Fig. 2. (a) τ_{rad} of a SiC sphere of radius $0.0125 \mu\text{m}$, (b) relative errors. Blue crosses: numerical results for a coarse mesh, red circles: numerical results for a fine mesh, black curve: analytical results. (For interpretation of the references to color in this figure legend, the reader is referred to the web version of this article.)

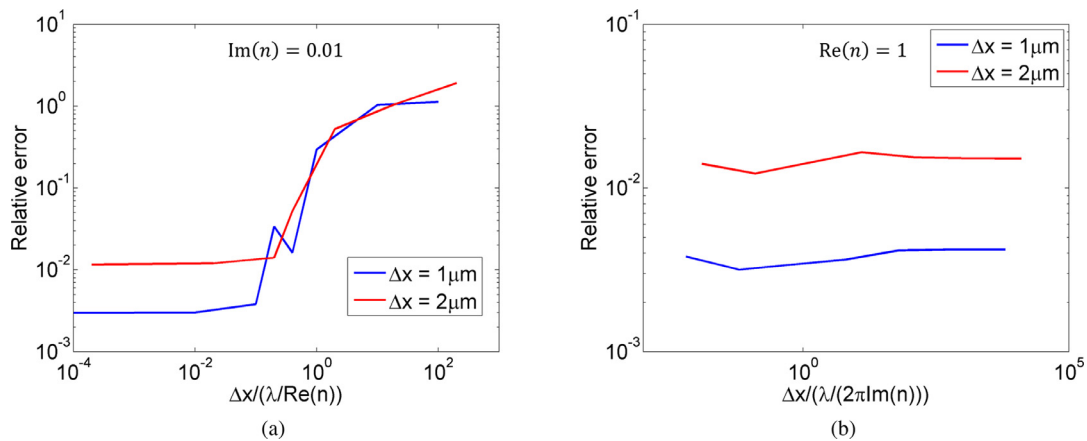


Fig. 3. Relative errors of τ_{rad} as a functions of (a) $\Delta x/(\lambda/\text{Re}(n))$, $\text{Im}(n) = 0.01$ with $\text{Re}(n)$ from 10^{-3} to 10^3 and (b) $\Delta x/(\lambda/(2\pi\text{Im}(n)))$ for $\lambda = 10 \mu\text{m}$, $\text{Re}(n) = 1$ with $\text{Im}(n)$ from 10^{-2} to 10^4 . Blue line: numerical results for a coarse mesh, red line: numerical results for a fine mesh. (For interpretation of the references to color in this figure legend, the reader is referred to the web version of this article.)

time shows a large increase (1.5 h per frequency instead of 3 min). Therefore, the mesh should be sufficiently fine to obtain a good convergence but not too fine to avoid a large computational time or numerical cancellation errors (see Fig. 2). Fig. 3 shows that for a given mesh size, the imaginary part of the optical index has a negligible influence on the convergence. Following Fig. 3a, the mesh size should be twice smaller than $\lambda/\text{Re}(n)$ to obtain a precision of numerical results within 5%. This points to difficulties for metallic

objects as they possess large real parts of the optical indices, in contrast to dielectric materials.

2.2. Thermal transfer between two spheres

Considering two objects labelled 1 and 2 at two temperatures T_1 and T_2 respectively, the net heat flux transferred between two objects is defined by the difference between the heat power emit-

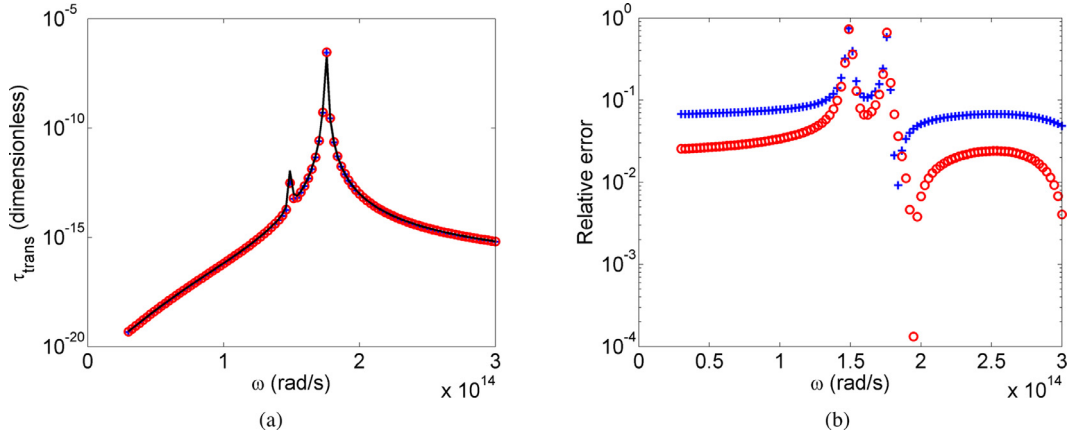


Fig. 4. (a) τ_{trans} of SiC spheres of radius $0.1 \mu\text{m}$ with a center-center distance of $10 \mu\text{m}$, (b) relative errors. Blue crosses: numerical results for a coarse mesh, red circles: numerical results for a fine mesh, black curves: reference results obtained by the asymptotic formula. (For interpretation of the references to color in this figure legend, the reader is referred to the web version of this article.)

ted by object 1, absorbed by object 2 and vice-versa:

$$Q_{\text{transfer}} = \int_0^{\infty} (\Theta(\omega, T_1) - \Theta(\omega, T_2)) \tau_{\text{trans}}(\omega) d\omega, \quad (2)$$

where τ_{trans} denotes the temperature-independent transmission [27]. Analytical methods [13] and numerical techniques [4,29] were developed for the computation of heat transfer between two spheres. If the sphere radius is very small compared to the distance d between two spheres and to the thermal wavelength, the transferred power can be approximated by [13,27,30–32]:

$$Q_{\text{transfer}} \simeq \frac{2}{\pi} \int_0^{\infty} (\Theta(\omega, T_1) - \Theta(\omega, T_2)) \times \sum_{P, P'} (\text{Re}\mathcal{T}_1^P + |\mathcal{T}_1^P|^2) (\text{Re}\mathcal{T}_1^{P'} + |\mathcal{T}_1^{P'}|^2) \times \left(\frac{9c^2}{2\omega^2 d^2} + \frac{9c^4}{2\omega^4 d^4} + \frac{27c^6}{2\omega^6 d^6} \delta_{P, P'} \right) d\omega \quad (3)$$

where P and P' denote the polarizations associated to two spheres and $\delta_{P, P'}$ is the Kronecker symbol of these polarizations. This asymptotic formula will be considered as a reference to validate SCUFF-EM.

Two SiC spheres of radius $0.1 \mu\text{m}$ are considered. The distance between the centers of the two spheres is $10 \mu\text{m}$. Since this distance is large compared to the sphere radius, it is possible to use Eq. (3) to compute reference results. The sphere mesh presented in Section 2.1 is used.

Fig. 4a represents the reference (black curve) and numerical results. Blue crosses and red circles are the numerical results obtained respectively for the coarse and fine meshes. We note that τ_{trans} shows two maxima close the SiC resonances ($\omega \simeq 1.5 \times 10^{14} \text{ rad.s}^{-1}$ and $\omega \simeq 1.75 \times 10^{14} \text{ rad.s}^{-1}$). The numerical results are in good agreement with reference results, but Fig. 4b still indicates that the error can be as high as 80% close to the resonances. Far from the resonances, convergence of numerical results is observed by decreasing the mesh.

3. Numerical modeling of sphere-substrate radiative heat transfer

The previous section only considered finite-size objects such as spheres. The objective of this section is to compute the radiative heat transfer between a sphere and a semi-infinite planar substrate using SCUFF-EM. This case is close to the tip-substrate configuration and was thoroughly investigated by analytical and numerical methods [14,18]. As SCUFF-EM is based on the boundary element

method and therefore can only be applied for modelling finite-size objects, the substrate is approximated by a cylinder of sufficiently large radius and thickness. In the end, our goal is to investigate the dependence of the total transferred flux on near-field gaps.

We consider a SiO_2 sphere of $0.8 \mu\text{m}$ radius and a SiO_2 substrate. The temperatures of the sphere and of the substrate are 400 K and 300 K respectively. When the distance between the surfaces of the two objects is not varying, it is set at $0.1 \mu\text{m}$. This case has already been presented in Ref. [18] by applying the T-DDA method.

3.1. Cylinder mesh requirements in the near field

Meshes of the two objects are represented in Fig. 5a. Since the near-field heat transfer is mainly in the region where the two objects are the closest to each other, meshes are refined in these regions in order to obtain accurate results. However, let us remark that an abrupt change of the mesh element size should not be introduced in order to avoid some numerical problems. Indeed, some tests (not presented here) showed that the implementation of an irregular mesh on the cylinder surface (see Fig. 5b for instance) leads to wrong results. A solution is to apply a linearly-varying mesh following $\Delta x = 0.09 r$ where Δx is the mesh size and r is the position of the element from the center of top surface.

We now turn to an analysis of the meshing of the cylinder. As the method is based on the Boundary Element Method, a precise meshing of the whole object is in principle required. However, in the near field, the SCUFF-EM results are well computed although the mesh of cylinder bottom surface does not satisfy the far-field convergence criterion shown in Section 2.1. This is because the near-field radiative heat transfer is a proximity effect. This relaxes the harsh criterion, which would be difficult to consider for large objects. This remark allows us to avoid a heavy mesh and a large computational time. In this respect, near-field computations involving large objects will be easier than far-field calculations. In the following, the bottom surface is computed with few discrete elements (60 elements, as the maximal mesh size of the bottom surface is set to be $R_c/2$) and the side meshing is also coarse, as shown in Fig. 5a. We found that both the bottom and the sides do not impact the exchanged flux.

3.2. Cylinder size and meshing

The geometrical approximation of the substrate by a cylinder is now under study. For each distance between the sphere and cylinder, the numerical convergence will be studied for different

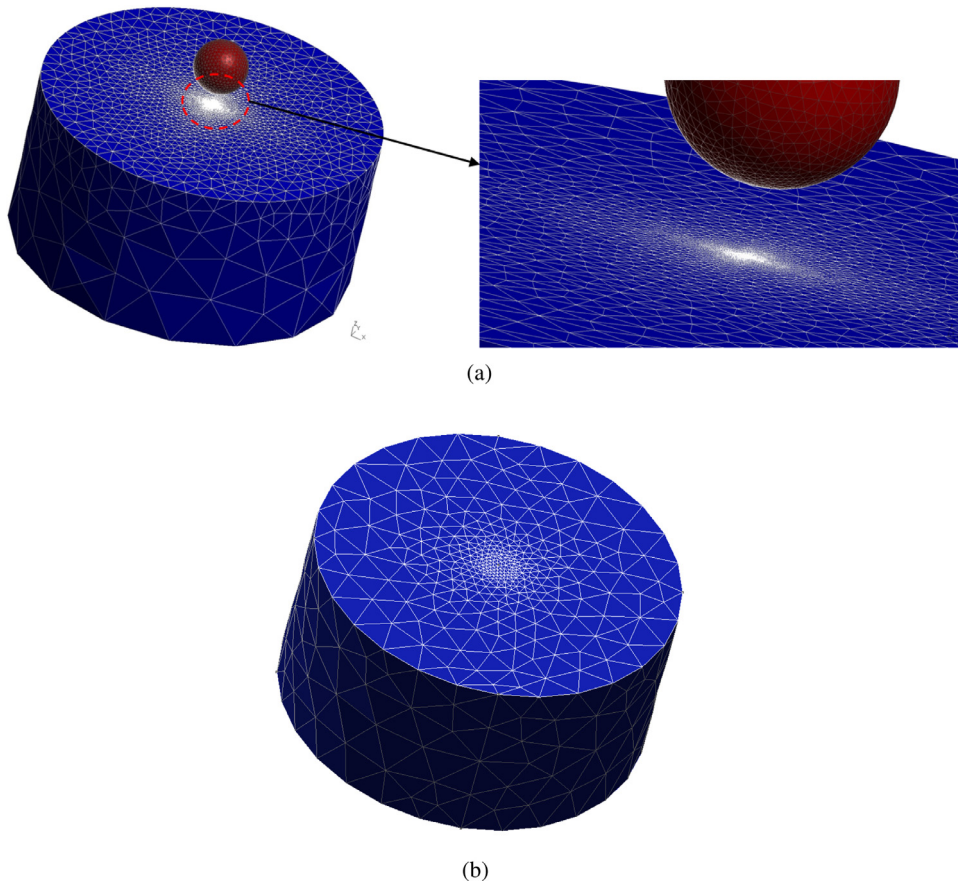


Fig. 5. (a) An example of non-uniform meshes for the sphere and cylinder and its zoom, (b) an example of irregular refined mesh of the cylinder which may yield numerical problems.

Table 1
Mesh information and computational time at $\omega = 0.919 \times 10^{14} \text{ rad.s}^{-1}$ for each cylinder size of Fig. 6.

$R_c = H_c$ (μm)	100	80	60	40	20	10	5	2
Nodes	2819	2700	2542	2303	1957	1615	1265	867
Edges	8448	8091	7617	6900	5862	4836	3786	2592
Computational time	18h54	16h53	15h03	12h00	8h20	5h40	3h19	1h48

sizes of cylinder and the finesse of cylinder mesh in order to determine the optimal configuration. The exchanged spectral flux is then computed and compared to analytical results to validate SCUFF-EM.

The convergence of numerical results is studied at a given frequency $\omega = 0.919 \times 10^{14} \text{ rad.s}^{-1}$, close to the first resonance of the SiO_2 dielectric function. First, the influence of the cylinder size on numerical results is analyzed. In order to decrease the number of degrees of freedom, we only consider the case where the cylinder radius is equal to its thickness in the following. This choice may not be the optimal one but as the lateral sides do not require precise meshing (as shown in Fig. 5), it will only lead to a slight increase of the computation time (if any). The sphere mesh consists of 777 nodes and 2322 edges with the mesh element size typically varying from $0.1 \mu\text{m}$ to $0.125 \mu\text{m}$. The cylinder radius and thickness change from $100 \mu\text{m}$ to $2 \mu\text{m}$. Table 1 indicates the node and edge numbers associated to the cylinder mesh and the computational time per frequency for each case. The minimal and maximal mesh sizes of the top surface are $0.1 \mu\text{m}$ and $R_c/10$ respectively with linear profile evolution between these extrema. Fig. 6a provides numerical results of the transferred spectral flux (blue curve) and analytical results (black line) as a function of cylinder radius. Numerical results converge to semi-analytical results as the cylinder

Table 2
Mesh information and computational time at $\omega = 0.919 \times 10^{14} \text{ rad.s}^{-1}$ for each cylinder size for Fig. 7.

Δx_{\min} (μm)	0.01	0.025	0.05	0.1	0.2	0.4
Nodes	2821	2303	1957	1615	1265	951
Edges	8454	6900	5862	4836	3786	2844
Computational time	18h39	12h06	8h24	5h33	3h25	2h09

size increases. Following Fig. 6b, the relative error is proportional to R_c^{-1} . The radius and thickness of the cylinder should be larger than $10 \mu\text{m}$ to obtain an accuracy better than 1% for the numerical results.

The effect of size of the cylinder mesh on the numerical convergence is now considered. As a result of the previous study, the optimal cylinder size (radius and thickness) is set to $10 \mu\text{m}$. The minimal mesh size Δx_{\min} of cylinder top surface mesh varies from $0.01 \mu\text{m}$ to $0.4 \mu\text{m}$. The node and edge numbers of the cylinder mesh and the computational time for one frequency are shown in Table 2 for each Δx_{\min} . Fig. 7a represents the numerical results of the spectral transferred flux (blue curve) and analytical results (black curve). We observe that refining the mesh improves the numerical accuracy. Fig. 7b shows that the relative error is propor-

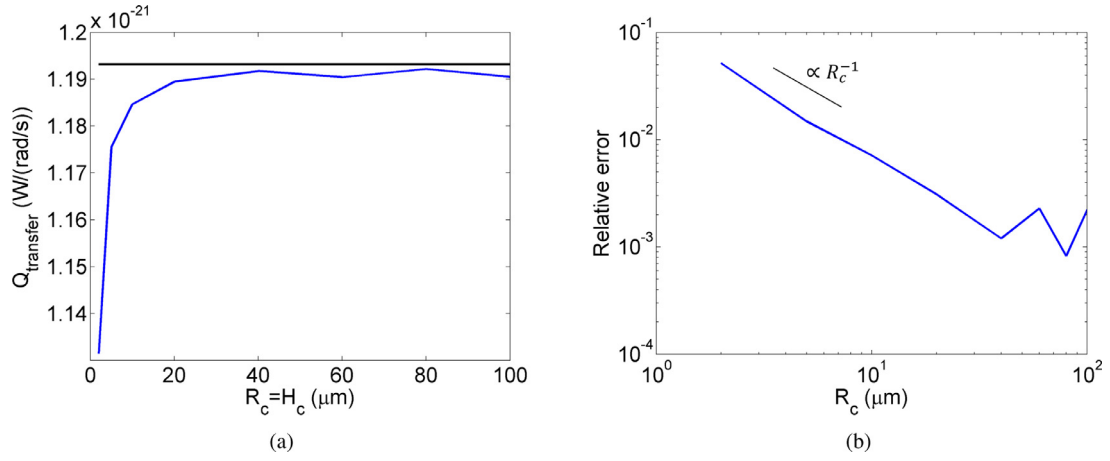


Fig. 6. Effect of the cylinder size. (a) Spectral exchanged power between a SiO₂ sphere and a SiO₂ cylinder at $\omega = 0.919 \times 10^{14}$ rad.s⁻¹, (b) relative errors. The sphere radius is 0.8 μm and the surface-surface distance between two objects is 0.1 μm. Black curve: analytical results, blue curve: SCUFF-EM results. (For interpretation of the references to color in this figure legend, the reader is referred to the web version of this article.)

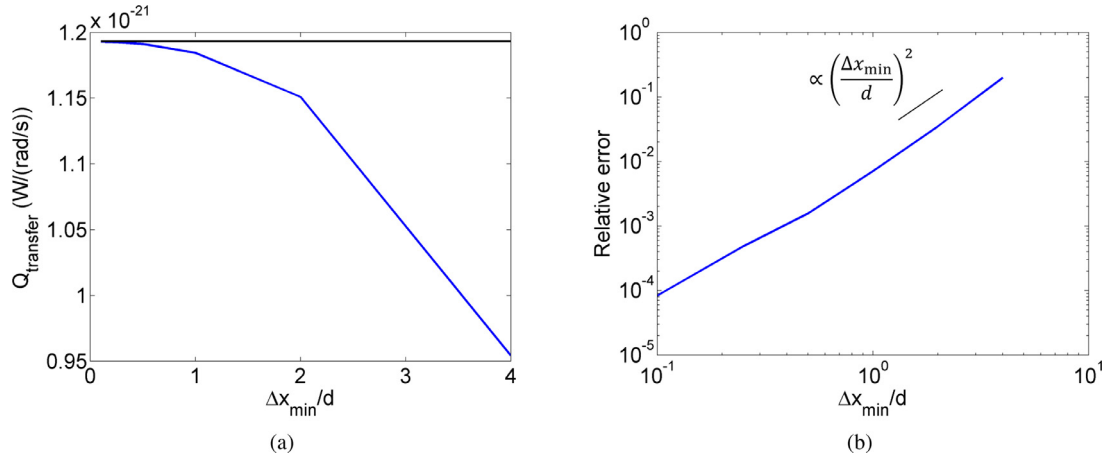


Fig. 7. Effect of the mesh on both sphere and substrate surfaces. (a) Spectral exchanged power between a SiO₂ sphere and a SiO₂ cylinder at $\omega = 0.919 \times 10^{14}$ rad.s⁻¹, (b) relative errors. The sphere radius is 0.8 μm, the cylinder radius and thickness are 10 μm, the surface-surface distance between two objects is $d = 0.1$ μm. Black curve: analytical results, blue curve: SCUFF-EM results. (For interpretation of the references to color in this figure legend, the reader is referred to the web version of this article.)

tional to $(\Delta x_{\text{min}}/d)^2$. The minimal mesh size of the cylinder mesh should be smaller than the separating distance in order to obtain an accuracy better than 1%.

Summing up the results, a 1% accuracy requires an optimal cylinder size of 10 μm for a separating distance of 0.1 μm and an optimal mesh of the cylinder containing 1615 nodes and 4836 edges. The top surface mesh is refined at the center with the mesh size varying from 0.1 μm to 1 μm. We note that the mesh of the top surface satisfies the convergence criterion in the far-field computation presented in Section 2.1. The computational time for each frequency is about 5h40.

The previous study points to the difficulties of numerical computation for very large or very small separating distances. Indeed, computation for very large separating distances requires a huge cylinder to obtain good convergence, which takes a long computational time. On the other hand, for a very small distance, the mesh is required to be very much refined and the mesh element size becomes too small compared to wavelength, which induces not only a long computational time but also numerical cancellation errors as explained in Section 2.1.

We have seen in Section 2 that the numerical computations close to the resonances of the dielectric function can lead to lower accuracies in the far field. In order to analyse the full spectrum, Fig. 8a represents the transferred spectral flux obtained by

the Boundary Element Method (blue curve), the semi-analytical method taken as reference [14] (black curve) and by the T-DDA method [18] (red curve). The relative errors are represented in Fig. 8b. A reasonable agreement between numerical and analytical results can be observed with a relative error up to 30% for Boundary Element Method results. Following Fig. 8b, the SCUFF-EM results are better than those of T-DDA in the low-frequency range and also around the two resonances of SiO₂ permittivity ($\omega \approx 10^{14}$ rad.s⁻¹ and $\omega \approx 2.2 \times 10^{14}$ rad.s⁻¹). However, the computation times of the two numerical techniques are not identical, so it is not possible to establish which one is the best.

3.3. Effect of the separating distance on the total transferred flux

We now study the influence of the separating distance on the total exchanged power between a sphere and a planar substrate. Table 3 shows the optimal cylinder size and the optimal element size of the cylinder mesh to obtain an error lower than 1% for each distance. We note that the 1% accuracy can be achieved only when the distance is larger than $d = 5$ nm as the numerical errors obtained for very small mesh/wavelength ratios (smaller than 2 nm) mentioned in Section 2.1 take place at the lower frequency. Fig. 9a and b represent respectively the spectral and the total transferred flux for different separating distances. The evolution of the

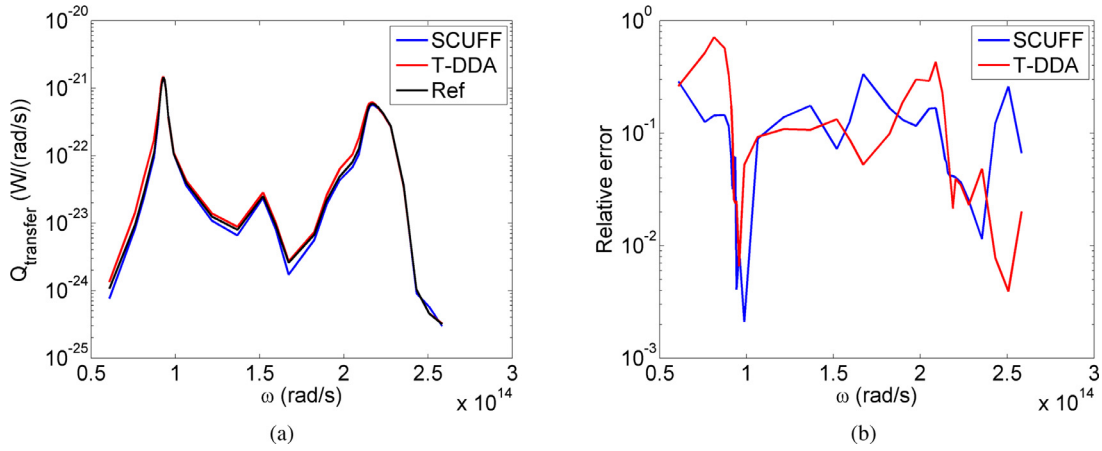


Fig. 8. Comparison between numerical methods. (a) Spectral exchanged power between a sphere and a cylinder, (b) relative errors. The sphere radius is $0.8 \mu\text{m}$, the cylinder radius and thickness are $10 \mu\text{m}$, the surface-surface distance between two objects is $0.1 \mu\text{m}$.

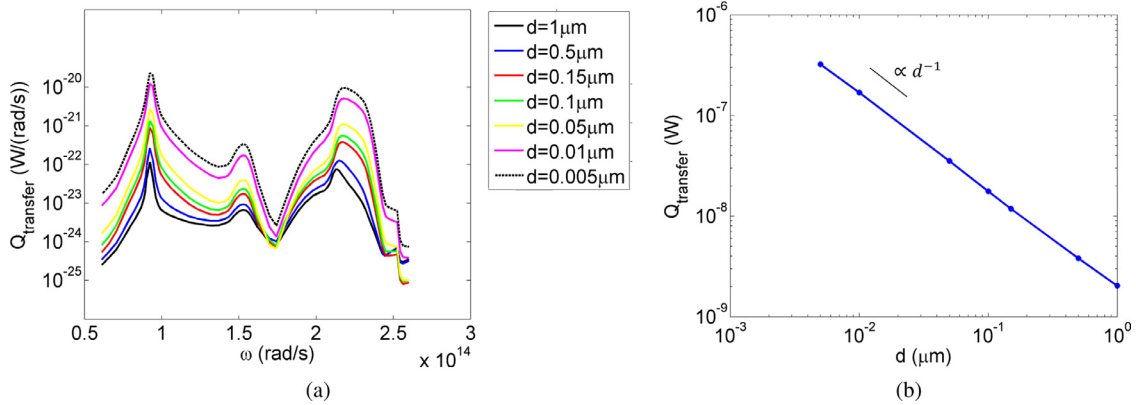


Fig. 9. Effect of sphere-substrate distance. (a) Optimal cylinder size and cylinder mesh refining for each separating distance, (b) spectral and (c) total exchanged power between a SiO_2 sphere and a SiO_2 cylinder for different distances between both objects. The sphere radius is $0.8 \mu\text{m}$.

Table 3

Optimal cylinder size and element size of the cylinder mesh for each separating distance in Fig. 9.

d (μm)	0.005	0.01	0.05	0.1	0.15	0.5	1
$R_c = H_c$ (μm)	0.8	1	5	10	10	60	100
Δx_{min} (μm)	0.005	0.01	0.05	0.1	0.125	0.125	0.125

spectrum as the tip-sample distance decreases is well reproduced. We confirm that the total exchanged power is proportional to $1/d$ for very small separating distance (near field). This behavior is no longer correct for larger distances (see e.g. Ref. [24]).

4. Numerical modeling of tip-substrate heat transfer

The objective of this section consists in computing radiative heat transfer between a tip and a sample in scanning thermal microscopy [3]. The probe tip of the microscope is heated and then placed near the cold substrate surface. Fig. 10 shows three probe geometries commonly used in experiments. The first one is a conical shape and the second one is a pyramid with a square base, as for the KNT tip [33,34]. The heights of these tips are smaller than $5 \mu\text{m}$ and their apexes may be rounded. Fig. 10c shows the last probe geometry which consists of an etched Wollaston wire bent in its middle part with a length of $200 \mu\text{m}$ [35]. While the first two probes could be implemented, the size of the Wollaston probe makes it difficult to deal with as it needs to meet both near-field

and far-field requirements. Note also that it is made of a metallic alloy, which requires a fine mesh.

In this section, we consider a test case which consists in computing the heat exchanged between a SiO_2 rounded conical tip and a SiO_2 infinite planar substrate. Note that the KNT probe is made of SiN and not anymore of SiO_2 . As SiO_2 was used in recent experiments, this choice will help comparing the results with actual experiments. As in Section 3, the substrate is approximated by a cylinder. An example of the tip and cylinder meshes are represented by Fig. 11. The cylinder mesh is the same as the one presented in the previous section. The cylinder and tip meshes are locally refined in the region where tip-sample separation is smallest, to ensure the accuracy of numerical results. First, numerical convergence will be studied as a function of different cylinder sizes and the size of the smallest cylinder mesh element in order to determine the optimal configuration of the cylinder. The objective is to find a solution which requires a reasonable computational time and provides accurate numerical results for a given separating distance. The exchanged spectral flux is then computed for different distances and the dependence of the total flux on the distance in the near field is highlighted.

In the considered case, the tip apex is a spherical cap. The tip aperture angle is 60° and the height of the tip is chosen arbitrarily to be $1.3 \mu\text{m}$. The cylinder radius is supposed to be equal to its thickness. Temperatures of the tip and cylinder are respectively 425 K and 310 K .

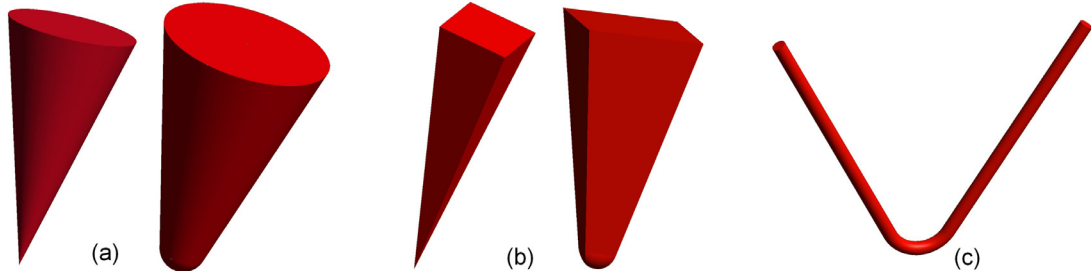


Fig. 10. Three geometries of probe tip with and without rounded apices. (a) Cone with disk base, (b) with square or rectangular base. (c) Heating part of the “Wollaston wire” probe.

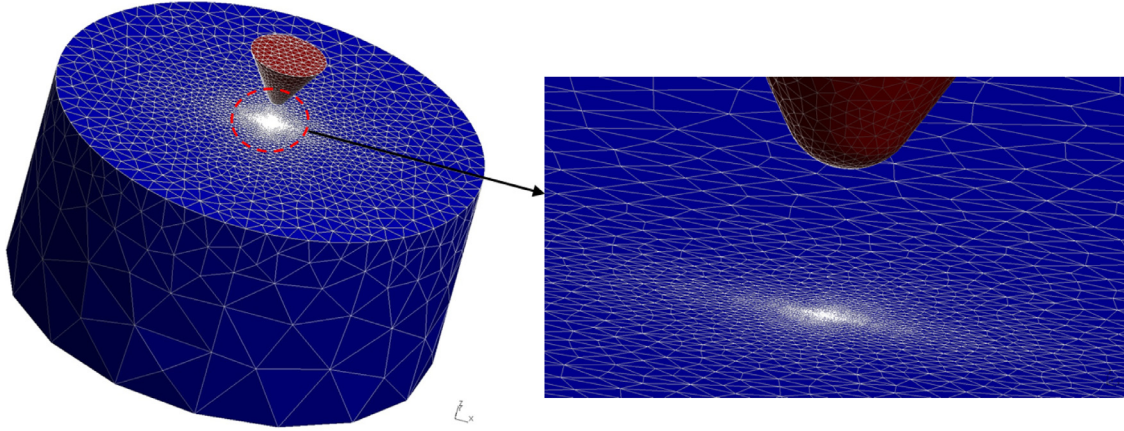


Fig. 11. An example of meshes of the cylinder and rounded conical tip and its zoom.

Table 4

Mesh information and computational time at $\omega = 0.919 \times 10^{14} \text{ rad.s}^{-1}$ for each cylinder size for Fig. 12.

$R_c = H_c$ (μm)	100	80	60	40	20	10	5	2
Nodes	2819	2700	2542	2303	1957	1615	1265	867
Edges	8448	8091	7617	6900	5862	4836	3786	2592
Computational time	17h48	15h57	13h58	11h18	7h47	5h11	3h8	1h37

4.1. Numerical requirements

The spherical cap has a radius of curvature of 225 nm. Convergence of numerical results is studied at the frequency $\omega = 0.919 \times 10^{14} \text{ rad.s}^{-1}$. The minimal distance between the surfaces of the two objects is $0.1 \mu\text{m}$. The mesh size of the tip is about $0.047 \mu\text{m}$ at the apex and $0.17 \mu\text{m}$ at the base. The tip mesh consists of 703 nodes and 2094 edges. We select a mesh size of the tip apex small enough compared to the separating distance to avoid numerical errors.

First, the finite size effect of the cylinder on the numerical results is investigated. The cylinder size decreases from $100 \mu\text{m}$ to $2 \mu\text{m}$. The minimal and maximal mesh sizes of the cylinder tip surface are set to be $0.1 \mu\text{m}$ and $R_c/10$ respectively. The mesh size of the bottom surface is chosen to be $R_c/2$. Table 4 gives the node and edge numbers of the cylinder mesh and the computational time at a given frequency for each cylinder size. Fig. 12a shows the transferred spectral flux computed by SCUFF-EM as a function of cylinder size. The numerical results converge as the cylinder size increases. Fig. 12b represents the relative errors. As no semi-analytical results are known in this case, the numerical result for the largest cylinder $R_c = 100 \mu\text{m}$ is considered as a reference to quantify the numerical errors. This figure shows that the relative error is proportional to $R_c^{-1.6}$ in this case and the cylinder size should be at least $10 \mu\text{m}$ to get less than 1% error.

Table 5

Mesh information and computational time at $\omega = 0.919 \times 10^{14} \text{ rad.s}^{-1}$ for each cylinder size for Fig. 13.

Δx_{\min} (μm)	0.01	0.025	0.05	0.1	0.2	0.4
Nodes	2821	2303	1957	1615	1265	951
Edges	8454	6900	5862	4836	3786	2844
Computational time	17h37	11h8	7h56	5h10	3h7	1h52

The effect of refining the cylinder mesh on the numerical convergence is now considered. Following the previous study, the optimal cylinder size is set to be $10 \mu\text{m}$. Different minimal mesh sizes Δx_{\min} of the cylinder top surface are studied, from $0.01 \mu\text{m}$ to $0.4 \mu\text{m}$. The information related to the cylinder mesh and the computational times at a given frequency are shown in Table 5 for each Δx_{\min} . Fig. 13a represents the numerical results of the transferred spectral flux. Convergence is obtained by refining the mesh. Fig. 13b shows the relative error with the reference result chosen as the numerical result obtained for the most refined mesh ($\Delta x_{\min} = 0.01 \mu\text{m}$). The relative error is found to be proportional to $(\Delta x_{\min}/d)^{2.5}$. The minimal mesh size for the cylinder should be smaller than the separating distance in order to obtain less than 1% error. In the following, we will choose $\Delta x_{\min} = d$.

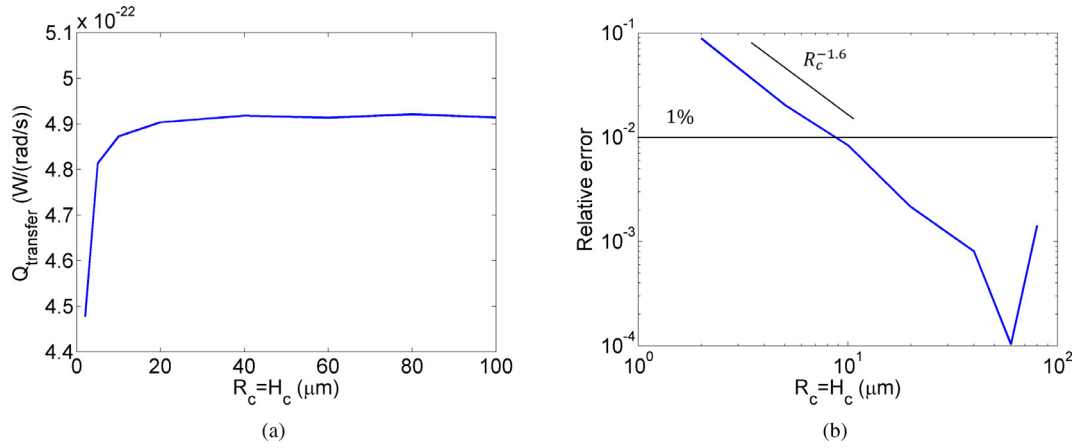


Fig. 12. Effect of the cylinder size. (a) Exchanged spectral power between a rounded conical tip and a cylinder at $\omega = 0.919 \times 10^{14} \text{ rad.s}^{-1}$, (b) relative error compared to the case where $R_c = H_c = 100 \text{ } \mu\text{m}$. The surface-surface distance between the two objects is $d = 0.1 \text{ } \mu\text{m}$.

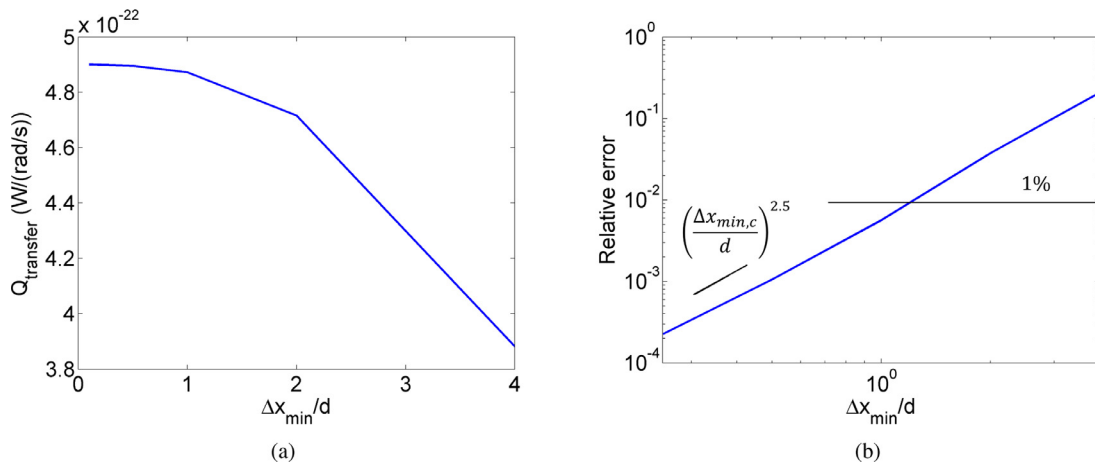


Fig. 13. Effect of the mesh size at both the substrate and the tip apex surfaces. (a) Exchanged spectral power between a SiO_2 rounded conical tip and a SiO_2 cylinder at $\omega = 0.919 \times 10^{14} \text{ rad.s}^{-1}$, (b) relative error compared to the case where $\Delta x_{\min} = 0.01 \text{ } \mu\text{m}$. The minimal surface-surface distance between the two objects is $d = 0.1 \text{ } \mu\text{m}$.

Table 6

Optimal cylinder size and element size of the cylinder mesh for each separating distance in Fig. 14.

d (μm)	0.004	0.02	0.1
$R_c = H_c$ (μm)	0.8	3	10
Δx_{\min} (μm)	0.004	0.02	0.1

4.2. Tip-sample radiative heat transfer for large radii of curvature

The same cone is considered in this case. While the 225 nm radius of its spherical cap can appear as large compared to other AFM probes which have radii of curvature as small as few nanometers, it ensures that no discretization errors are introduced. In addition, tip apexes of large curvature radii are usually used in experiments aiming at measuring near-field thermal radiation with scanning thermal microscopy [7,36], which are larger than those used in sharp AFM experiments.

4.2.1. Power exchange

As the cone-surface thermal power exchange diverges when the cone height increases, we set the cone height at $h = 1.3 \text{ } \mu\text{m}$. The near-field behavior of the tip-surface thermal transfer is analyzed by studying the influence of the separating distance on the transferred heat. As an example, Table 6 shows the optimal cylinder

size and the optimal size of the cylinder mesh for three distances $d = 0.004 \text{ } \mu\text{m}$, $0.02 \text{ } \mu\text{m}$ and $0.1 \text{ } \mu\text{m}$ in order to obtain relative errors lower than 1%. Fig. 14a and b represent the spectral and the total exchanged power of the sphere-surface (dashed curves) and the cone-surface (continuous curves) configurations for these separating distances. The sphere and the tip radii are the same. These figures show that for small gaps, the spectral and total heat transfer for the tip-substrate geometry become very close to the values of the sphere-substrate geometry. We find numerically that the total exchanged power is proportional to $d^{-0.9}$, close to the near-field behavior of the sphere-substrate thermal transfer found previously ($\propto d^{-1}$). It is interesting to observe that such tip would lead to a power transferred on the order of 145 nW at 4 nm, i.e. a thermal conductance of $1.26 \times 10^{-9} \text{ W.K}^{-1}$, which is about 10 times lower than that shown by Rousseau et al. [5] for the same material but not the same distance nor the same radius, 1.8 times larger than [7] for the same tip-sample distance but for a SiO_2 tip and a Si sample, and about the same order as that reported by Ref. [8] but neither for the same material nor the same tip apex radius. In comparison to the heat transferred through air [37], these values stay much lower. If only the rounded part of the tip is considered, a thermal conductance through air of approximately $1.5 \times 10^{-8} \text{ W.K}^{-1}$ can be estimated. However, the tip head and the cantilever are also known to contribute to the heat transfer [33,38] and the real conductance measured in experiments is larger.

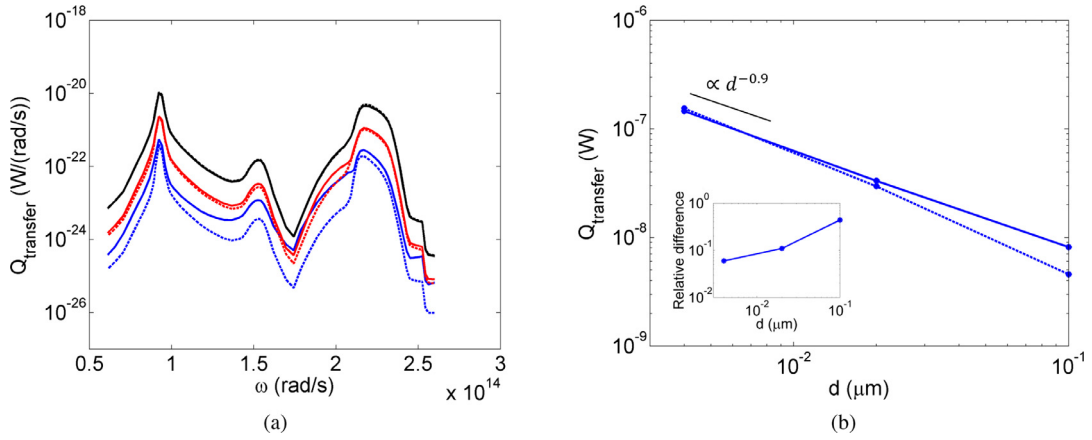


Fig. 14. (a) Spectral and (b) total exchanged power between a SiO₂ rounded conical tip (continuous curves) or a SiO₂ sphere (dashed curves) and a SiO₂ cylinder for different distances between two objects. Black, red and blue colors correspond to $d = 0.004, 0.02, 0.1 \mu\text{m}$ respectively. Dashed and continuous black curves appear superimposed. The tip height is $1.3 \mu\text{m}$, the tip aperture angle is 60° and the radii of the tip apex and of the sphere are $0.225 \mu\text{m}$. The inset represents the relative difference between the total tip-sample and sphere-sample exchanged powers. (For interpretation of the references to color in this figure legend, the reader is referred to the web version of this article.)

4.2.2. Spatial resolution

Fig. 15a and b show the spatial distribution of the temperature-independent transferred flux on the surface of each object computed at $\omega = 0.919 \times 10^{14} \text{ rad}\cdot\text{s}^{-1}$ for a tip-sample distance of 4 nm . We remind that the frequency selected is that of the first resonance. Fig. 15c represents the normalized spatial distribution of the radiative heat flux on the surfaces at four frequencies close to the first and third resonances. Fig. 15d shows the cumulative power curves ($P(\omega_0) = \int_{\omega=0}^{\omega_0} q(\omega) d\omega$ where q is the spectral power) for different separating distances d . Two large increases of the cumulative power at the vicinity of the first and third resonances show that these two resonances give the largest contributions to the spectral exchanged power. Therefore, the study of the exchanged power should be carried out for the whole spectrum instead of only first resonant frequency. However, the normalized spatial distributions at four frequencies close to these two resonances have similar profiles which is very much concentrated at the tip apex and at the center of the cylinder top surface. As a result, all the investigations at the first resonant frequency can provide the global point of view for the whole frequency spectrum.

We can define the spatial resolution of the near-field radiative heat transfer as the full width at half maximum (FWHM) of the profile of the heat flux absorbed by the sample. With this criterion we find values of 51 nm , 131 nm and 342 nm respectively for distances $4, 20$ and 100 nm (see Fig. 16). The spatial resolution seems to scale proportionally to $d^{1/2}$. We verified that for dielectrics in close proximity, the tip spherical cap-sample interaction can be assimilated locally to horizontal parallel elements as in the Proximity Flux Approximation (also called often the Derjaguin approximation by analogy with the works performed for the Casimir force) [24]. In this case, the power exchanged can be computed by integrating around the tip spherical cap:

$$P = \int_0^R \frac{C}{(d+z)^2} 2\pi r dr \quad (4)$$

where C/d^2 is the asymptotic expression of the exchanged power between two parallel flat surfaces, and z is the difference of height between an elementary surface of the sphere and the plane parallel to the sample surface at the tip extremity. Note that Eq. (4) is valid provided that $d+z$ is approximately lower than 170 nm for SiO₂ (see Ref. [39]). There is a deviation to this asymptotic expression for larger distances. Rousseau et al. proposed an expression for C in Ref. [40].

Eq. (4) shows that the shape of the flux received by the sample will be close to a lorentzian, but not exactly (see also Fig. 15c). In fact, the $d^{1/2}$ behavior observed numerically can be derived from such an expression. One finds that the full width at half maximum writes

$$\sigma = 2\sqrt{2(\sqrt{2}-1)Rd} \approx 1.82\sqrt{Rd}, \quad (5)$$

where R is the radius of curvature. This observation confirms that the tip-sample exchange is really local when the bodies are in proximity. However, for $d = 100 \text{ nm}$, part of the spherical cap of the tip lies outside of the regime of validity of Eq. (4). This explains the deviation (30%) between the spatial resolution estimated from Eq. (5) and the one observed numerically. Another limitation to Eq. (5) may enter into play: the shape of the tip becomes conical at some distance from the apex, deviating from the spherical shape. Assuming no sharp angle at the connection between the conical part and the spheroidal one (*i.e.* the sphere is cut at some angle α from the horizontal direction), we can show that this sets a limit to Eq. (5) for $d_0 = R \cos(\alpha) / [2(\sqrt{2}-1)]$. In the computations, an angle of 30° between the vertical direction and the tip side has been considered, so that $d_0 \sim 0.9R$. As our radius of curvature is large, this criterion is not relevant. However, it can become significant for smaller radii. Note also that this derivation is only valid for dielectrics, and that the behavior may be very different for metals where a leveling-off is predicted [6,31]. While the radius and tip material are different to those of [41], the results can be compared to the values found in the experiments by scanning surface steps. The experimental resolution of [41], achieved with a sharper tip, appears smaller than the one highlighted here: reducing the radius of curvature decreases the spatial resolution.

4.3. Tip-sample radiative heat transfer for small radii of curvature

The influence of the separating distance on the transferred heat is now studied for a cone of smaller curvature radius. This study allows clarifying the effect of small radii of the tip apex on the exchanged power compared to the large radii. The curvature radius of the tip apex under consideration here is 50 nm . The conical tip height is the same as the one considered in the previous section ($h = 1.3 \mu\text{m}$). The cylinder sizes and the cylinder mesh sizes for three distances $d = 0.004 \mu\text{m}, 0.01 \mu\text{m}, 0.02 \mu\text{m}$ are shown in Table 7.

The spectral exchanged power for this cone-surface configuration is represented in Fig. 17a for these separating distances.

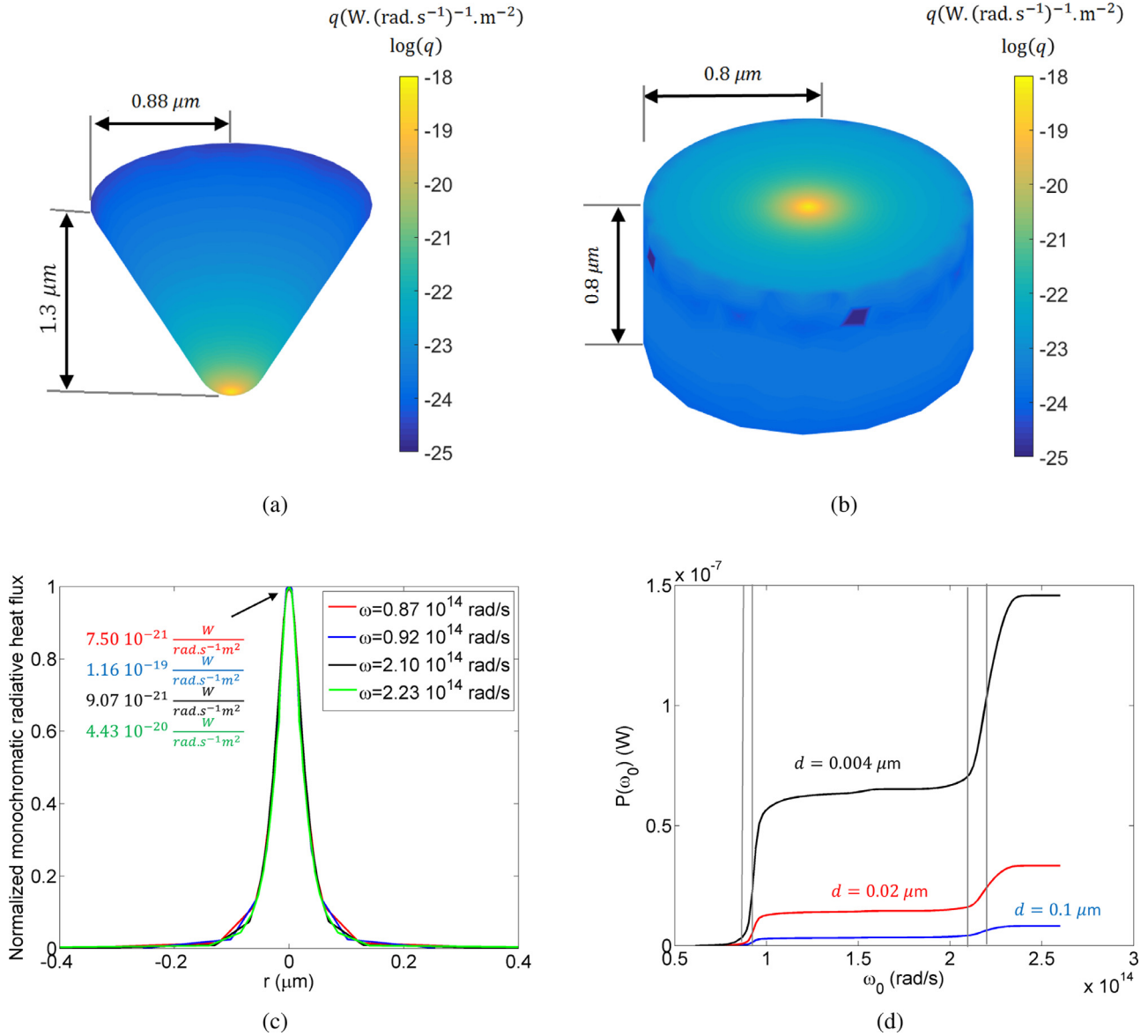


Fig. 15. Spatial distribution of the radiative heat flux q ($W \cdot (rad \cdot s^{-1})^{-1} \cdot m^{-2}$) of the transferred flux on the surfaces of (a) SiO₂ tip and (b) substrate, at $\omega = 0.919 \times 10^{14} \text{ rad} \cdot s^{-1}$. Note that the colormap is in logarithmic scale. (c) Normalized spatial distribution of the radiative heat flux q_{sample} on the top surface of the substrate with the colormap in the linear scale at different frequencies. The gap is $d = 4 \text{ nm}$. (d) Cumulative power curve $P(\omega_0) = \int_0^{\omega_0} q(\omega) d\omega$ for different separating distances, the four frequencies considered in (c), which are close to the resonances are denoted by four vertical lines.

Table 7

Cylinder size and element size of the cylinder mesh for each separating distance in Fig. 17.

d (μm)	0.004	0.01	0.02
$R_c = H_c$ (μm)	0.8	1.5	3
Δx_{min} (μm)	0.004	0.01	0.01

Fig. 17b compares the numerical results (blue curves) of the total exchanged power for the rounded cone with some analytical results for different shapes. The cyan and red curves correspond respectively to the contributions of the pure conical and the spherical parts of the tip. The black curve corresponds to the result obtained for the whole rounded conical tip while the green curve provides the data associated to a perfect cone of identical height and aperture angle. Fig. 18 summarizes the various shapes of the tips and the analytical formulae obtained within the frame of the PFA following Eq. (4).

In the extreme near-field, when the separating distance is very small compared to the curvature radius of the tip, the total exchanged power of the spherical part of the cone, which is proportional to d^{-1} , becomes dominant. For a perfect cone, the half aperture angle of the tip α impacts the power exchanged through a factor $(\frac{R_c}{H})^2 = \tan^2 \alpha$ and the dependence of the power on the distance is logarithmic (see Fig. 18). One should remember that the PFA is valid in principle only for regions of the tip at distances smaller than 200 nm of the sample, so the contribution of the conical part might be slightly different than that given by Fig. 18. As a result, the behavior of the exchanged power should be softer than d^{-1} . The exponent of the power law d^{-n} found for the numerical data is $n = 0.78$. It can be conjectured that this exponent depends on both the radius of curvature of the tip and the aperture angle of the cone. Comparing the PFA and the numerical data, we find a reduction by a factor two for the computation. It could be estimated that the PFA of Eq. (4) provides a lower bound to the power exchanged, as shown e.g. by [14], but it is not the case here.

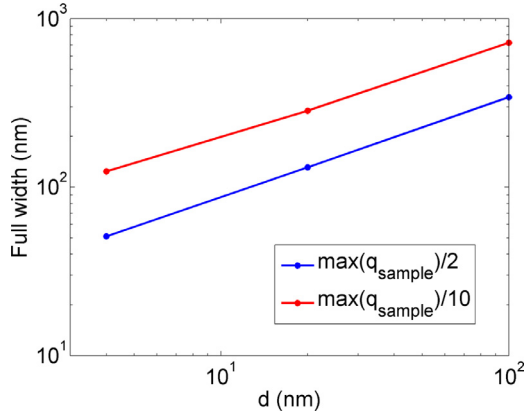


Fig. 16. Full width at half (blue curve) and 10% of maximum (red curve) of the spatial distribution of the heat flux q_{sample} absorbed by the sample as a function of distance between the tip and substrate. (For interpretation of the references to color in this figure legend, the reader is referred to the web version of this article.)

This underlines that the PFA might not be as accurate for sharp objects than for gently-curved ones.

Finally, we observe that the power exchanged for the small radius of curvature of 50 nm (3.72×10^{-8} W) is smaller by a factor 4 than the one exchanged for the large radius of curvature of 225 nm (1.46×10^{-7} W) at a distance 4 nm, and by a factor ~ 3 at 20 nm. This confirms that near-field thermal radiation experiments in the near-contact are easier with large radii of curvature and that the impact of the curvature radius decreases at larger distances.

5. Conclusion

In this work, we have introduced a step-by-step approach to compute near-field radiative heat transfer for simplified and realistic scanning thermal microscopy geometries. In a first step, we have approximated the probe tip by a sphere. In a second step, we have used a conical shape rounded at its apex. For each separating distance between the tip and the substrate and all objects sizes, the numerical convergence has been investigated to provide the criteria required to reach a given accuracy. The dependence of heat transfer on the separating distance has also been analyzed for

a dielectric material. While the total near-field exchanged heat is proportional to d^{-1} for the sphere-plane geometry, we find close behaviors for rounded cone-plane configuration with large curvature radius of the cone apex. For smaller curvature radii of the cone apex, the behavior of the exchanged power is softer and can be written as d^{-n} with $n < 1$. Our data allow to compare the radiative heat flux and the flux exchanged through air, and to determine the spread of the radiative flux, i.e. its spatial resolution which can scale as \sqrt{d} .

Future work could include additional aspects related to the geometry of experiments. For instance, surface roughness of the probe tip and substrate can also be taken into account (see e.g. Supplementary information of [7]). More importantly, the cantilevers of some of the probes could influence the radiative heat exchange. From the numerical point of view, each geometry and material presents its own advantages and difficulties. As an example, the KNT tip [33,34] is made of silicon nitride and the dielectric function of the SiN tip is not well known as experimental data are scarce in literature. Doped Si was also implemented in resistive probes [42] and its permittivity depends on the doping levels. An advantage of conical and pyramidal tips is that their heights are fixed and smaller than $5 \mu\text{m}$, which does not require much computational memory. However, the curved zone of their rounded shapes is difficult to define. One advantage of the Wollaston tip is that it is made of a homogeneous material, a situation easily handled by SCUFF-EM. However, its large aspect ratio makes it difficult to simulate totally: its length is about $200 \mu\text{m}$ with a cross-section radius of $2.5 \mu\text{m}$. In addition, the permittivity may require to be determined. Contrarily to the conical and pyramidal tips, the Wollaston probe is metallic and requires a very fine mesh to ensure accurate numerical results. This leads to large computational time and resources, close to or beyond the limits available currently. Moreover, it is known that the Wollaston probe is not isothermal, contrarily to the tips considered in this study. The simulations considered here should therefore be extended for anisothermal objects. This is feasible if the temperature distribution on the surfaces of the objects is known, as it is usually the case. Indeed, the transmittivity between pairs of discretized elements is computed within the SCUFF-EM code. Finally, let us mention that it is now time to apply these results to compute the tip-sample near-field heat transfer with nanostructured samples, which should bring a

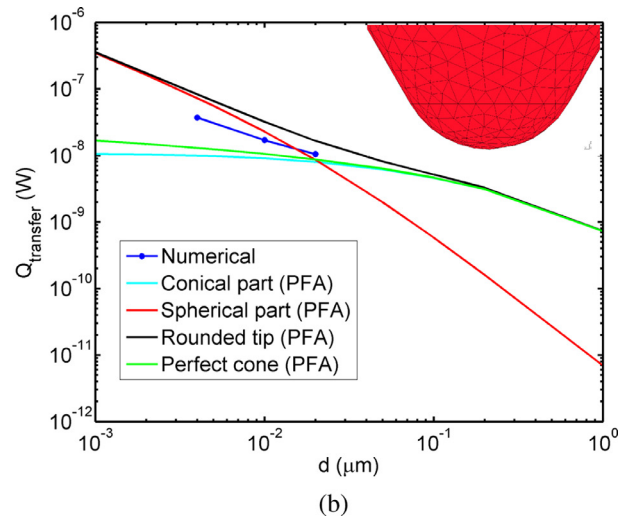
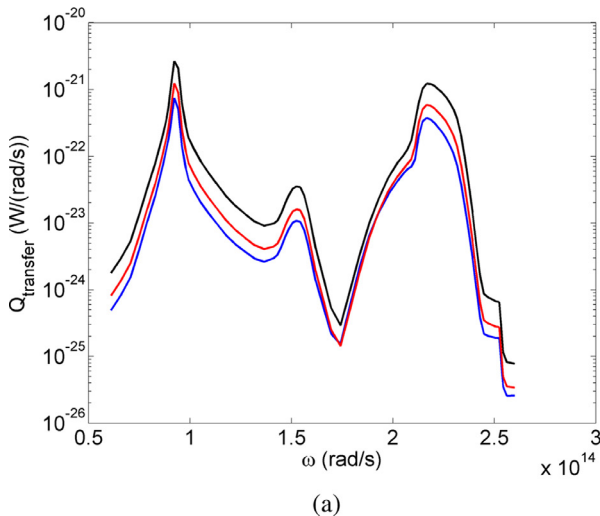


Fig. 17. (a) Spectral and (b) total exchanged power between a SiO₂ rounded conical tip and a SiO₂ cylinder for different distances between two objects. Black, red and blue colors correspond to $d = 0.004, 0.01, 0.02 \mu\text{m}$ respectively. The tip height is $1.3 \mu\text{m}$, the tip aperture angle is 60° and the radii of the tip apex and of the sphere are 50 nm . (For interpretation of the references to color in this figure legend, the reader is referred to the web version of this article.)

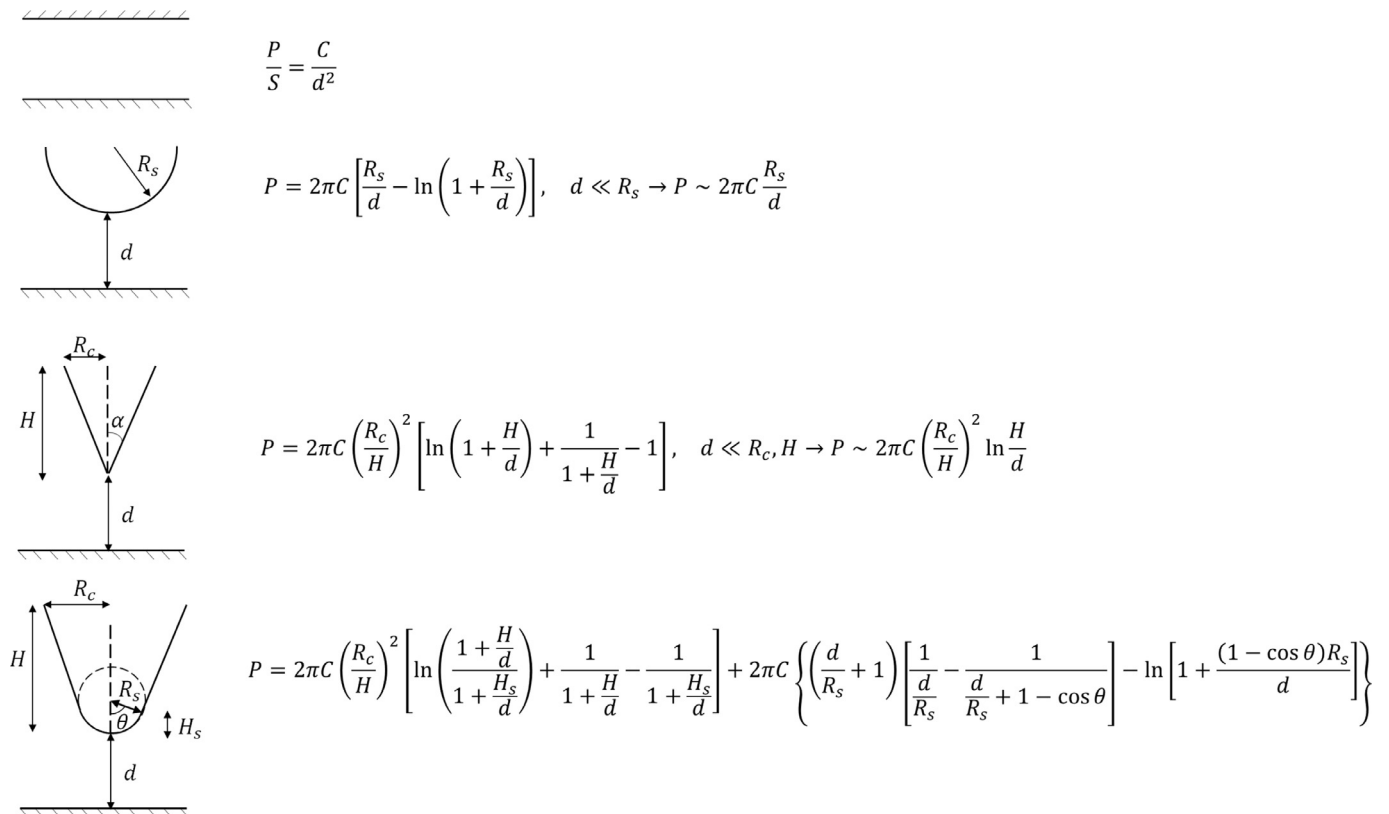


Fig. 18. Analytical expression of the total exchanged power of two infinite surfaces, of the sphere-surface and of the cone-surface configurations in the frame of the Proximity Flux Approximation.

breadth of novel interesting results as it has done in fields such as near-field plasmonics [43].

Acknowledgments

The authors acknowledge the support of projects EU FP7-NMP-2013-LARGE-7 Quantiheat, ANR Demo-NFR-TPV and INSA BQR REDCAV. Heavy computations were performed thanks to the P2CHPD center for computational resources of Fédération Lyonnaise de Modélisation et Sciences Numériques. The authors are grateful to R. Vaillon for early discussion and interesting comments, to M. Francoeur (Univ. of Utah) for providing us reference and T-DDA results, and to P. Klapetek for useful tests of the SCUFF-EM code at the CMI facilities. The authors also thank M.T. Homer Reid and coworkers for releasing SCUFF-EM and answering questions on the associated web forum.

References

- [1] Planck M. *The Theory of Heat Radiation*. P. Blakiston Son & Co; 1914.
- [2] Xu JB, Lauger K, Moller, Dransfeld K, Wilson IH. Heat transfer between two metallic surfaces at small distances. *J Appl Phys* 1999;76(11). doi:10.1063/1.358001.
- [3] Gomes S, Assy A, Chapuis P-O. Scanning thermal microscopy: a review. *Phys Status Solidi A* 2015;212(3):477–94.
- [4] Narayanaswamy A, Chen G. Thermal near-field radiative transfer between two spheres. *Phys Rev B* 2008;77:075125.
- [5] Rousseau E, Siria A, Jourdan G, Volz S, Comin F, Chevrier J, et al. Radiative heat transfer at the nanoscale. *Nature Photonics* 2009;3:514–17.
- [6] Kittel A, Muller-Hirsch W, Parisi J, Biehs S-A, Reddig D, Holthaus M. Near-field heat transfer in a scanning thermal microscope. *Phys Rev Lett* 2005;95:224301.
- [7] Kim K, Song B, Fernandez-Hurtado V, Lee W, Jeong W, Cui L, et al. Radiative heat transfer in the extreme near field. *Nature* 2015;528:387–91.
- [8] Kloppstech K, Konne N, Biehs S-A, Rodriguez AW, Worbes L, Hellmann D, et al. Giant near-field mediated heat flux at the nanometer scale. *Nat Commun* 2017;8:14475.
- [9] Song B, Fiorino A, Meyhofer E, Reddy P. Near-field radiative thermal transport: from theory to experiment. *AIP Adv* 2015;5(053503):1–47.
- [10] Wilde YD, Formanek F, Carminati R, Gralak B, Lemoine P-A, Joulain K, et al. Thermal radiation scanning tunnelling microscopy. *Nature* 2006;444:740–3.
- [11] Babuty A, Joulain K, Chapuis P-O, Greffet J-J, de Wilde Y. Blackbody spectrum revisited in the near field. *Phys Rev Lett* 2013;110:146103.
- [12] Polder D, Van Hove M. Theory of radiative heat transfer between closely space bodies. *Phys Rev B* 1971;4:3303.
- [13] Volokitin AI, Persson BNJ. Radiative heat transfer between nanostructures. *Phys Rev B* 2001;63:205404.
- [14] Otey C, Fan S. Numerically exact calculation of electromagnetic radiative heat transfer between a dielectric sphere and plate. *Phys Rev B* 2011;84:245431.
- [15] Carrillo LY, Bayazitoglu Y. Nanorod near-field radiative heat exchange analysis. *J Quant Spectrosc Radiative Transfer* 2011;112(3):412–19.
- [16] Datas A, Hirashima D, Hanamura K. FDTD Simulation of near-field radiative heat transfer between thin films supporting surface phonon polaritons: lessons learned. *J Thermal Sci Technol* 2013;8(1):91–105.
- [17] Edalatpour S, Francoeur M. The thermal discrete dipole approximation (t-dda) for near-field radiative heat transfer simulations in three-dimensional arbitrary geometries. *J Quant Spectrosc Radiative Transfer* 2014;133:364–73.
- [18] Edalatpour S, Francoeur M. Near-field radiative heat transfer between arbitrarily-shaped objects and a surface. *Phys Rev B* 2016;94:045406.
- [19] <https://github.com/HomerReid/buff-em>.
- [20] Polimeridis AG, Reid MTH, Jin W, Johnson SG, White JK, Rodriguez AW. Fluctuating volume-current formulation of electromagnetic fluctuations in inhomogeneous media: incandescence and luminescence in arbitrary geometries. *Phys Rev B* 2015;92:134202.
- [21] Rodriguez AW, Homer Ried MT, Johnson SG. Fluctuating-surface-current formulation of radiative heat transfer for arbitrary geometries. *Phys Rev B* 2012;86:220302(R).
- [22] Homer Reid MT, Johnson SG. Efficient computation of power, force, and torque in BEM scattering calculations. *IEEE Trans Antennas Propag* 2015;63(8):3588–98.
- [23] Joulain K, Ben-Abdallah P, Chapuis P-O, Henkel C, Babuty A, et al. Strong tip-sample coupling in thermal radiation scanning tunneling microscopy. *J Quantit Spectrosc Radiative Transfer* 2014;136:1–15.
- [24] Chapuis P-O, Greffet J-J, Volz S. Near field radiative heat transfer between a sphere and a surface. In: *Proceedings of 13th international heat transfer conference*, Sydney, Australia, (2006); 2006.
- [25] Rodriguez AW, Homer Ried MT, Johnson SG. Fluctuating-surface-current formulation of radiative heat transfer: theory and applications. *Phys Rev B* 2013;88:054305.
- [26] Kattawar GW, Eisner M. Radiation from a homogeneous isothermal sphere. *Appl Opt* 1970;9(12):2685–90.

- [27] Krüger M, Bimonte G, Emig T, Kardar M. Trace formulas for nonequilibrium casimir interactions, heat radiation, and heat transfer for arbitrary objects. *Phys Rev B* 2012;86:115423.
- [28] Palik ED. *Handbook of Optical Constants of Solids*. Academic Press, Boston; 1985.
- [29] Sasihithlu K, Narayanaswamy A. Proximity effects in radiative heat transfer. *Phys Rev B* 2011;83:161406.
- [30] Domingues G, Volz S, Joulain K, Greffet J. Heat transfer between two nanoparticles through near field interaction. *Phys Rev Lett* 2005;94(8):085901.
- [31] Chapuis P-O, Laroche M, Volz S, Greffet J-J. Near-field radiative heat transfer between metallic nanoparticles. *Appl Phys Lett* 2008;92(20):201906.
- [32] Manjavacas A, García de Abajo FJ. Radiative heat transfer between neighboring particles. *Physical Review B* 2012;075466.
- [33] Ge Y, Zhang Y, Weaver JMR, Zhou H, Dobson PS. Topography-free sample for thermal spatial response measurement of scanning thermal microscopy. *J Vacuum Sci Technol B* 2015;33(6):06FA03.
- [34] http://www.kelvinnanotechnology.com/products/products_scanning_probes.html.
- [35] Pylkkä RJ, Moyer PJ, West PE. Scanning near-field optical microscopy and scanning thermal microscopy. *Jpn J Appl Phys* 1994;33:3785.
- [36] Cui L, Joeng W, Fernández-Hurtado V, Feist J, García-Vidal F J CJC, Meyhofer E, et al. Study of radiative heat transfer in Ångström- and nanometre-sized gaps. *Nat Commun* 2017;8(14479):1–9.
- [37] Massoud A.M., Bluet J.-M., Chapuis P.-O. Air contribution in calibrated microprobe-based scanning thermal microscopy.
- [38] Park K, Cross GLW, Zhang ZM, King WP. Experimental investigation on the heat transfer between a heated microcantilever and a substrate. *Journal of Heat Transfer* 2008;130(10):102401.
- [39] Mulet JP, Joulain K, Carminati R, Greffet JJ. Enhanced radiative heat transfer at nanometric distances. *Microscale Thermophys Eng* 2002;6:209–22.
- [40] Rousseau E, Laroche M, Greffet J-J. Asymptotic expressions describing radiative heat transfer between polar materials from the far-field regime to the nanoscale regime. *J Appl Phys* 2012;111(1):014311.
- [41] Kittel A, Wischnath UF, Welker J, Huth O, Rütting F, Biehs S-A. Near-field thermal imaging of nanostructured surfaces. *Appl Phys Lett* 2008;93:193109.
- [42] King WP, Kenny TW, Cross KEGG, Despont M, Dürig U. Atomic force microscope cantilevers for combined thermomechanical data writing and reading. *Appl Phys Lett* 2001;78:1300–2.
- [43] Gramotnev DM, Bozhevolnyi SI. Plasmonics beyond the diffraction limit. *Nature Photon* 2010;4:83–91.